ORIGINAL RESEARCH ARTICLE

Effect of Strain Hardening on Wear and Corrosion Resistance of 316L Austenitic Stainless Steel

Guoqing Sun, Jiaqi Huang, Jian Peng, and Wangping Wu

The wear and corrosion resistance of 316L austenitic stainless steel after strain hardening were studied. 316L austenitic stainless steel was composed of a large amount of austenite and a small fraction of martensite. After strain hardening at room temperature, the contents of phases were not changed basically. With the increase of pre-strain deformation, the microhardness of the surface and cross-section slightly increased, and the microhardness of the sample with pre-strain deformation of 20% was the largest. When the pre-strain deformation was greater than 5%, the surface microhardness was greater than the cross-sectional microhardness. The dynamic average friction coefficients of the stainless steel after pre-strain deformation of 0%, 5%, 10%, and 20% were 0.67, 0.57, 0.2, and 0.12, respectively. The friction coefficient of the samples gradually decreased with the increase of strain hardening. The wear resistance of 316L stainless steel was improved after pre-strain deformation. The steel with pre-strain deformation of 20% had a small abrasive scratch depth and low friction coefficient, which exhibited good wear resistance. The corrosion resistance of the samples after strain hardening deteriorated for the initial state without immersion due to the existence of defects. The corrosion resistance of the sample with pre-strain deformation of 5% after soaking for 3 days was the best, compared with the other as-strained samples.

1. Introduction

Austenitic stainless steel has outstanding self-passivation ability, comprehensive mechanical properties, and good processability, which is widely used in machinery, petrochemical, nuclear power, vessel boat, medical and pressure vessel (Ref 1). The mechanical strength of stainless steel can be increased by strain hardening (Ref 2). When the stainless steel is loaded to a certain plastic cold deformation at room temperature and then unloaded, the yield strength of the steel will be improved. The pre-strain improved the yield strength of austenitic stainless steel, but the wall thickness was reduced, and the lightweight of pressure equipment was realized (Ref 3). Lee et al. (Ref 4)

reported that the microstructure of 304L steel changed obviously after pre-strain treatment, and found that the increase of dislocation density, twin density, and the volume fraction of martensite influenced the compressive flow stress.

Many studies on austenitic steels have been provided in various kinds of literatures, which focused on the wear and corrosion behaviour of austenitic steels. Parthasarathi and Duraiselvam (Ref 5) studied the wear rate of austenitic stainless steel at high temperature and claimed that the oxide layer began to form at 350 °C and more. Hua et al. (Ref 6) studied the friction and wear behaviors of 304 austenitic stainless-steel disc against Al_2O_3 ceramic ball and GCr15 bearing steel ball, respectively. They found that the specific wear rate of the steel decreased with the increasing of the sliding speed, and the wear of the steel was a mixing mode of both adhesion and plough processes. Li et al. (Ref 7) investigated the mechanoelectrochemical effect of austenitic stainless steel in an acid chloride solution and found that the non-uniform strain at the initial stage of strain ($\varepsilon_p < 0.05$) had a great influence on corrosion resistance. Tokita et al. (Ref 8) studied the welded austenitic stainless steels with different compositions and found that variations in their microstructure (generation of precipitated phases) significantly affected the pitting corrosion performance. Meanwhile, the redistribution of elements caused significant differences in intergranular corrosion susceptibility. Kumar et al. (Ref 9) reported the microstructure and hot corrosion performance of wire-arc additive manufacturing processed 321 stainless steel in molten salt and air environments. They found the formation of cracks in the corroded surface because of the oxides fluxing by sulfur and vanadium. Wen et al. (Ref 10) evaluated the influence of heat input on the microstructural features and localized corrosion performance of an austenitic stainless steel manufactured by wire-arc additive manufacturing. The corrosion behaviour of additive manufactured steel

Guoqing Sun and **Jiaqi Huang**, Electrochemistry and Corrosion Laboratory, School of Mechanical Engineering and Rail Transit, Changzhou University, Changzhou, People's Republic of China; **Jian Peng**, Jiangsu Key Laboratory of Green Process Equipment, Changzhou University, Changzhou 213164, People's Republic of China; and **Wangping Wu**, Electrochemistry and Corrosion Laboratory, School of Mechanical Engineering and Rail Transit, Changzhou University, Changzhou, People's Republic of China; and Jiangsu Key Laboratory of Green Process Equipment, Changzhou University, Changzhou 213164, People's Republic of China. Contact e-mails: wwp3.14@163.com and wuwping@cczu.edu.cn.

became low, which was attributed to the segregation of Mo and Cr within the Ni-poor δ-ferrite regions.

After strain hardening, the mechanical properties of 316L stainless steel can be improved dramatically to some extent. However, few publications report on the wear and corrosion resistance of the steel after strain hardening. In addition, the local corrosion easily occurred at the surface of the steel in the corrosion solution (Ref 11, 12). Lindroos et al. (Ref 13) studied the mechanical properties and wear resistance of a chromium-alloyed high-manganese austenitic steel and found that the increase in strain rate resulted in an increase in the yield strength, and the pre-strain had a wear-decreasing effect against impacts when the pre-strain deformation was below 30%. Ko et al. (Ref 14) demonstrated that the friction force and the friction coefficients of hardened steel-on-martensitic grade stainless steel under sliding friction conditions increased with the increase of external loading. The phenomenon was caused by the combined effect of phase transformation and material hardening in the steel. Xu et al. (Ref 15) illustrated that the friction within high sliding speed conditions for austenitic steel could produce: (i) α' martensite, (ii) equiaxed dislocation of the sub-surface, and (iii) a hardening effect. The corrosion resistance of 304L stainless steel in simulated groundwater containing chloride ions depended on chemical composition, grain size, inclusions, microstructure, thermal or heat treatment, sensitization, secondary precipitates, and weld defects (Ref 16-21). Gopinath et al. (Ref 22) reported the effect of cryo-rolling (CR) on the phase transformation of 304L steel and found that metal subjected to CR had high dislocation density. The dislocation density increased with increasing CR, and corrosion initiation was easily favored at the deformation region. Hsu et al. (Ref 23) also discovered that cold rolling was detrimental to the corrosion resistance of 304L steel since the rolling process caused the introduction of slip bands and martensite in the steel, and pitting was easy to occur at the intersection of the slip line.

In previous works (Ref 24-27), the yield strength of 316L steel increased after strain hardening, but the elongation evidently decreased with pre-strain deformation, and tensile strength basically remained constant. The effect of pre-strain on mechanical behaviour is related to dislocation accumulation and mechanical twinning. In this study, the microstructure, microhardness, wear resistance, and corrosion resistance of 316L stainless steel with different degrees of strain hardening were studied and compared with original sample of 316L stainless steel.

2. Experimental

2.1 Preparation

The chemical composition of 316L stainless steel is displayed in Table 1 (Ref 24). The tensile specimen had a gage length of 35 mm, a width of 10 mm and a thickness of 3 mm. The small samples (10 x 10 x 3 mm) were cut by a wire cutting machine from the middle region of the tensile specimens after strain hardening (See Fig. 1), and then carefully polished with 1500 grit SiC papers. The tensile specimens were operated at room temperature at a constant strain rate of 5 x 10^{-4} s^{-1}, pre-deformed to 5% (represented as sample #1), 10% (sample #2), and 20% (sample #3). The original sample was not pre-deformed, namely sample #0. The polished parts were etched with aqua regia solution, then cleaned with acetone solution, and dried. The calculation formula of pre-strained value (ε_{pre}) is given as follows (Ref 27):

$$\varepsilon_{pre} = \frac{L_{pre} - L_0}{L_0} \tag{Eq 1}$$

where L_{pre} is the initial gauge length of the pre-strained sample, and L_0 is the initial gauge length of the as-received sample.

2.2 Characterizations

The metallographic morphologies and abrasive scratches of the samples were observed by optical microscopy (OM, VHX-700F). The phase identification of the top-surface of sample was identified by x-ray diffraction (XRD, APEX II DUO) with Cu-Kα radiation by two times.

2.3 Microhardness

The microhardness values of the surface and cross-section of the samples were tested with an HVS-52 Vickers hardness tester with a load of 1.0 kg under a holding time of 15 s. The microhardness values were performed at fifteen times and the final value was averaged.

2.4 Wear Resistance

The surface friction coefficient of the samples was measured by HSR-2 M-type high-speed reciprocating friction and wear tester with Si$_3$N$_4$ ceramic ball with a diameter of 5 mm. The friction mode was sliding, and the running conditions were a load of 5 N, a rotation speed of 500 rpm, a running time of 30 min, a moving length of 5 mm, and a working temperature of 25 °C.

2.5 Corrosion Resistance

The electrochemical corrosion resistance of the steel part was evaluated in 3.5 wt% NaCl solution by potentiodynamic polarization and electrochemical impedance spectroscopy (EIS) techniques using an electrochemical workstation (CHE 660E, Shanghai Chenhua, China). The sample was coated with insulating adhesive to expose an area of 1 cm^2. A three-compartment glass cell was used, a Pt counter electrode, and an Ag/AgCl 3.0 M KCl reference electrode. The sample was used as the working electrode. The samples were immersed in the beaker for different soaking times, including 0 h, 1 h, 3 h,

Table 1   Chemical composition of 316L stainless steel

Element	C	Si	Mn	P	S	Cr	Mo	Ni	Fe
wt.%	0.022	0.47	1.07	0.024	0.001	18.5	2.13	11.0	Bal.

10 h, 24 h, and 72 h. Here, the immersing time of 0 h indicated that the samples were immersed in 3.5 wt% NaCl solution for 30 min after the steady-state open circuit potential (OCP) and EIS tests. Firstly, the steady-state OCP value was tested in solution for 10 min. Then, EIS measurements were carried out after the steady-state OCP value was achieved by applying a voltage signal of 10 mV in a frequency of $10^{-2} \sim 10^{5}$ Hz. Potentiodynamic polarization was finally tested at a scanning rate of 10 mV s^{-1}. The EIS data were fitted by Zsimpwin software.
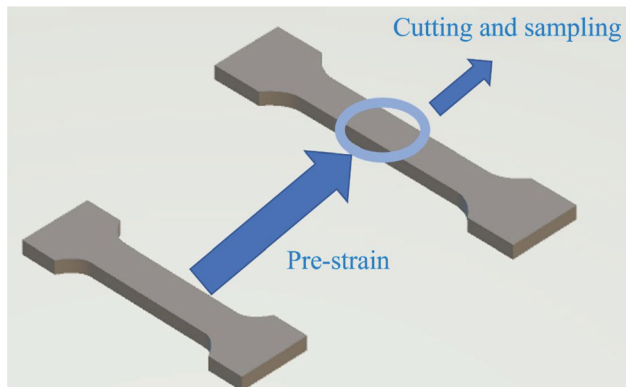

Fig. 1 Pre-strain schematic diagram

3. Results

3.1 Characterization

Figure 2 shows the XRD patterns of the samples with and without strain hardening. After the pre-strain deformation, the relative intensity and position of the diffraction peaks for austenite phase were basically the same while the relative intensity of the diffraction peak for martensite phase had some changes. According to a previous study (Ref 25), the dislocation density increased with a pre-strained value for 316L stainless steel. The stainless steels from original and as-strained samples were composed of a large amount of γ austenite and a small fraction of α' martensite. The content of martensite and austenite after strain hardening was calculated from the integrated intensities of martensite and austenite phases in the XRD patterns by the following Eq 2, 3 and 4 (Ref 28):

$$V_\alpha = \frac{I_\alpha}{I_\alpha + 0.942 I_\gamma} \tag{Eq 2}$$

$$V_\gamma = \frac{1.4 I_\gamma}{I_\alpha + 1.4 I_\gamma} \tag{Eq 3}$$

$$V_\alpha + V_\gamma = 1 \tag{Eq 4}$$

where I_α represents the integrated intensity of the (110) diffraction peak of martensite phase, and I_γ is the integrated intensity of the (111) diffraction peak of austenite phase. According to formulas 2, 3 and 4, the percent volume of α' martensite for samples #0, #1, #2, and #3 was $16.15 \pm 2.05\%$, $14 \pm 3.53\%$, $15.31 \pm 0.014\%$, and $13.2 \pm 4.6\%$ respectively and the austenite was $83.85 \pm 2.05\%$, $86 \pm 3.53\%$, $84.69 \pm 0.014\%$, and $86.8 \pm 4.6\%$, respectively.
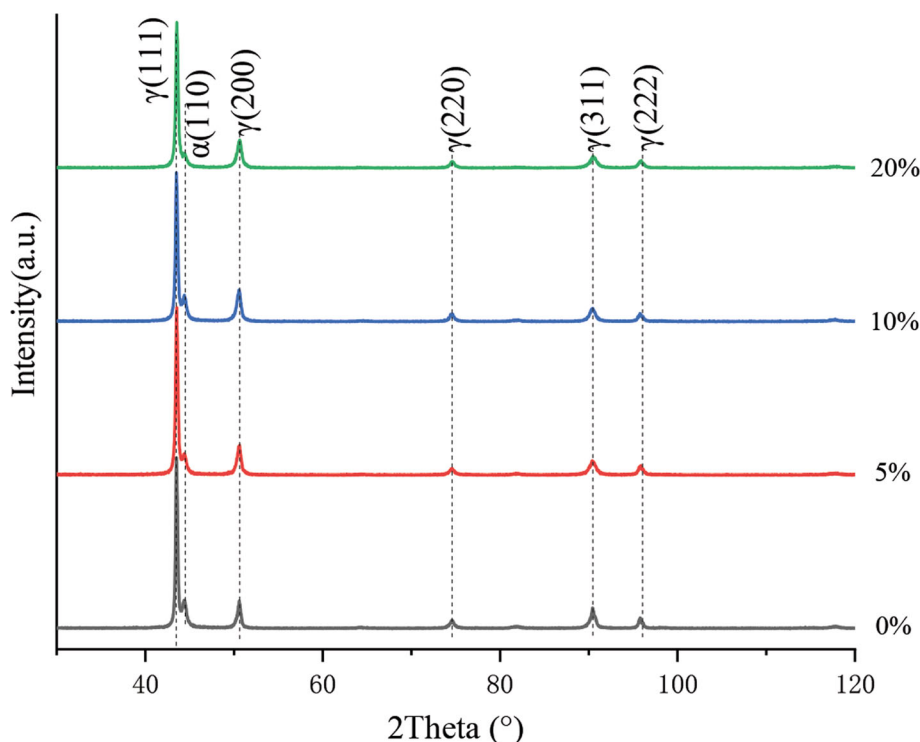

Fig. 2 XRD patterns of the samples with pre-strain deformation

Figure 3 displays the metallographic micrographs of the surface of samples. The twining band boundaries of the metallographic phase are shown in the original sample #0 (Fig. 3a). With the increase of pre-strain value, mechanical twins (Fig. 3b), and a twinning phenomenon appeared (Fig. 3c and d) (Ref 25). The dislocations and twin boundaries were induced by deformation, which could help to enhance the atomic diffusion rate (Ref 29). The high pre-strained samples showed notably more grains with a high number of localized slip lines and twins than the samples with low pre-strain value, but the distribution and spacing of the grains in the samples with high pre-strain value were less uniform than those in the
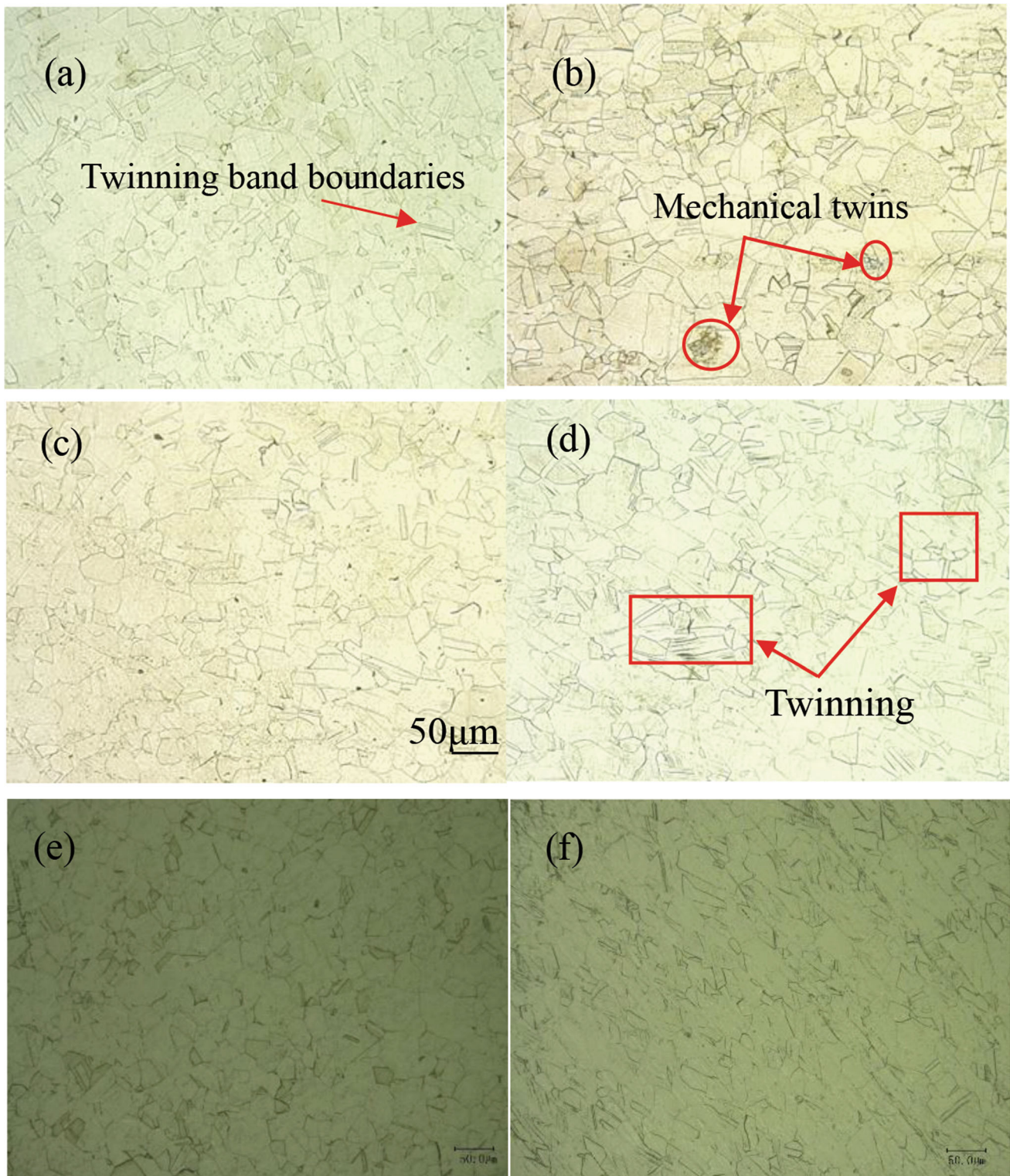

Fig. 3 Metallographic micrographs of surface of the samples with pre-strain deformation of (a) 0%, (b) 5%, (c) 10%, (d) 20%, and metallographic micrographs of cross-section of the samples with pre-strain deformation of (e) 0% and (f) 20% (Magnification × 500)

samples with low pre-strain value. In Fig. 3(a) and (b), the distribution of the large grain size of the surface was almost similar. However, after pre-strain deformation of larger 5%, the distribution of large grain size was less than that for samples #2 and #3. Furthermore, the cross-sectional metallographic micrographs of steels for samples #0 and #3 were studied and observed in Fig. 3(e) and (f), respectively. It can be carefully observed that the distribution of larger grain size in Fig. 3(e) was much more than that in Fig. 3(f), indicating that the large grain with similar equiaxed structure in the steel was deformed into finer microstructure after large pre-strain deformation of 20%. This interesting phenomenon could influence the microhardness of the steel.

3.2 Microhardness

Figure 4 shows the microhardness of the surface and cross-section of the samples. The average surface microhardness values of samples #0, #1, #2 and #3 were 173.8 ± 7.2 $HV_{1.0}$, 210.72 ± 3.1 $HV_{1.0}$, 238.5 ± 8.1 $HV_{1.0}$ and 298.88 ± 35.7 $HV_{1.0}$ respectively, while the average cross-sectional microhardness values were 210.18 ± 1.2 $HV_{1.0}$, 212.58 ± 1.2 $HV_{1.0}$, 232.12 ± 28.6 $HV_{1.0}$ and 239.52 ± 40.9 $HV_{1.0}$, respectively. Figure 4 shows that the hardness value of 316L steel slightly increases with increasing pre-strain and that the sample with the largest value of surface microhardness was sample #3, while the smallest was the original sample #0. The increase in hardness of the sample under pre-strain is the result of changes in dislocation organization within the material. With the increase in pre-strain for 316L austenitic stainless steel, the shear stress increases, thus prompting the dislocation substructure along the slip surface movement, in the process of deformation to varying degrees of lamellar dislocation, deformation twins, and the formation of dislocation plugging and dislocation cellular organization near the grain boundary and annealed twin boundary. All these structural changes produce a strengthening effect leading to an increase in hardness. The cross-sectional hardness of the sample increases gradually with increasing pre-strain value, but not as much as the surface hardness. The difference in the hardness values of the surface and cross-section of sample #0 might be ascribed to the effect of machining. However, the cross-sectional microhardness values of sample #1 were similar in magnitude to the surface microhardness values of the specimens, but the cross-sectional microhardness values of samples #2 and #3 were slightly smaller than the surface microhardness values of the samples, which were attributed to the crystallographic anisotropy of the samples after relatively large strain hardening and the deformation of grain size. Therefore, the cross-sectional microhardness increases with increasing pre-strain values due to the deformation in grain size (see Fig. 3e and f).

3.3 Wear Resistance

Figure 5 shows the dynamic friction coefficient curves against the running time for four samples. According to the development trend of friction coefficient curves, the friction coefficient curve can be divided into three stages: initial friction stage, running in fluctuation stage, and steady-state stage (Ref 6, 30). At the beginning of friction, the friction coefficients were rising, then entered the period of friction coefficient fluctuation, and finally reached the steady-state period of slow change. The dynamic average friction coefficients of samples 0#, 1#, 2#, and 3# were 0.67, 0.57, 0.2, and 0.12, respectively. The friction coefficient of the samples decreased with the increase of pre-strain hardening. There are two main ways to improve the wear resistance of stainless steel, including the reduction in friction and improvement in the deformation
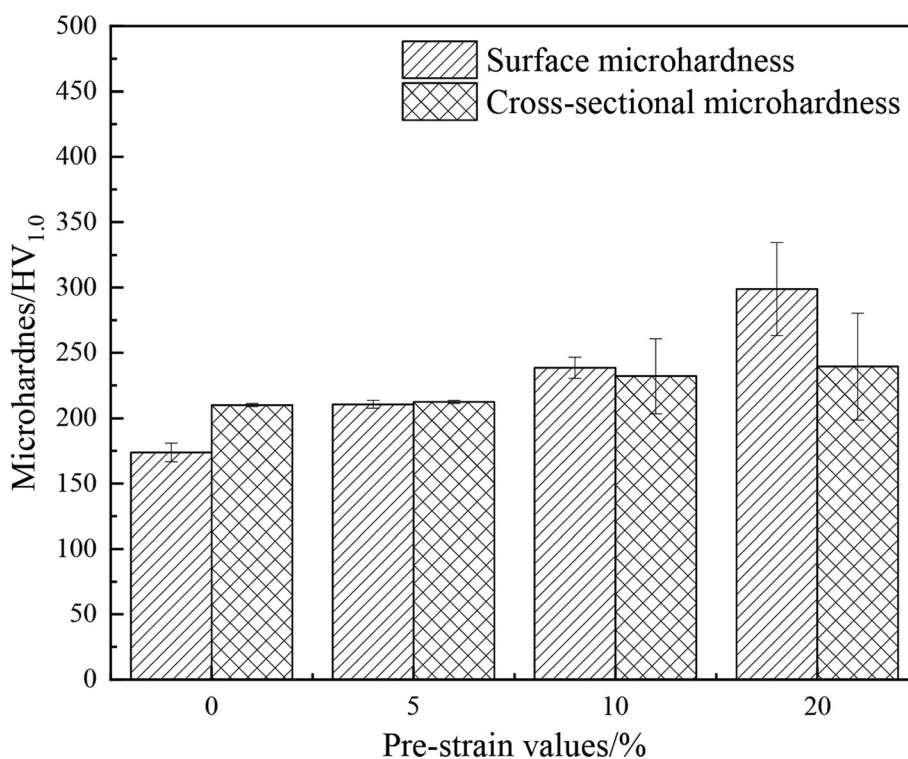

Fig. 4 Microhardness of top-surface and cross-section of samples with pre-strain deformation
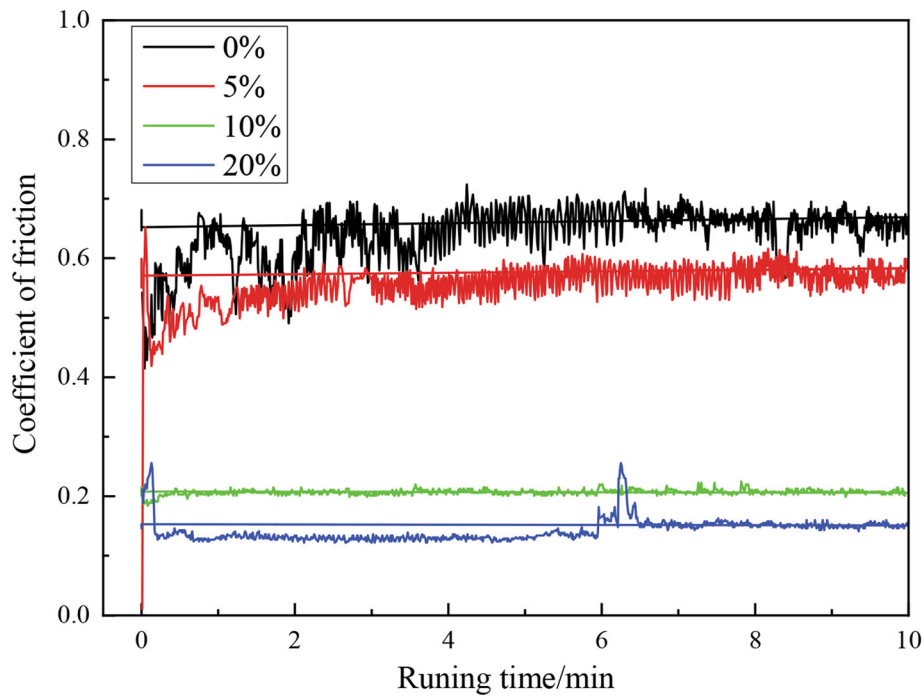
Fig. 5 Surface friction coefficients of samples with and without pre-strain deformation

resistance of the surface of stainless steel (Ref 31). Therefore, the wear resistance of the stainless steel was significantly improved after strain hardening due to the increase in the surface and cross-sectional microhardness, which was in agreement with the results from Ko et al. (Ref 14) and Xu et al. (Ref 15).

Figure 6 shows the optical micrographs of the surface morphology of the abrasion scratches of samples with and without pre-strain deformation. The surface morphology of the scratches for as-strained samples changed significantly compared to original sample. Under the same loading and movement speed, there was no large amount of shedding on the surface of the samples. The wear scar of the original sample was wide, and there were a large number of uneven flake deposits on the surface of the wear scratch (Fig. 6a and b), indicating that serious adhesion occurred. The wear scar of sample #1 began to narrow, but there was still some adhesion phenomenon (Fig. 6c and d). The wear scratches of sample #2 were slight, and there was basically no adhesion, but there were abrasive marks (Fig. 6e and d). The wear scar of sample #3 was smooth (Fig. 6g and h), with no adhesive tendency.

The surface of the original sample has a serious adhesion phenomenon because the hardness of austenitic stainless steel is lower than that of the friction pair ball. During the friction process, there was adhesion transfer between the friction pairs, indicating that the wear mechanism of the original sample was mainly adhesive wear, and the wear mechanism of the treated samples was abrasive wear and adhesive wear. Riviere et al. (Ref 32) studied the sliding friction mechanism of austenitic stainless steel and found that the wear surface produced obvious wear and abrasion.

Figure 7 displays the contour plots of the samples with and without pre-strain deformation. Table 2 shows the depth and width of the scratches for the samples. The width of the as-strained samples was narrower compared with the original sample, indicating the wear resistance of samples with pre-

strain deformation was better than that of original sample #0. At the same time, the depth of sample #3 was only 3.135 μm, which was lower than those of the other samples. Combining the friction coefficient and scratch depth, 316L austenitic stainless steel with a pre-strain deformation of 20% has the best wear resistance.

3.4 Corrosion Resistance

Figure 8 shows the potentiodynamic polarization curves of the samples in 3.5 wt% NaCl solution. The corrosion potential (E_{corr}), corrosion current density (I_{corr}) and polarization resistance (R_p) of the samples are shown in Figure 8 and Table 3. The corrosion resistance of the sample is related to the E_{corr} and I_{corr} values. The E_{corr} value of sample #0 is the most negative, -0.30 V, and the E_{corr} value of sample #3 is the most positive, -0.16 V. With the increase of strain hardening, the maximum I_{corr} value is 3.82 μA/cm^2 when the pre-strain value is 5% for sample #1. The corrosion resistance of sample #2 for the immersion time of 0 h is better than that of other samples because sample #2 had low corrosion density and high R_p values. At the same time, we need to consider EIS data to analyze the corrosion performance.

From Figure 9, with the increase of immersion time, the E_{corr} value of sample #0 increased rapidly to -0.165 V for a soaking time of 1 h, then decreased rapidly, and then changed more smoothly (Fig. 9a). The I_{corr} value also increased rapidly to 21.21 μA/cm^2 for 1 h and then decreased rapidly (Fig. 9b). The E_{corr} value of sample 1# decreased slowly with increasing immersion time, then decreased rapidly to -0.223 V for 3 h, and then decreased slowly to -0.23 V, then increased rapidly after 10 h, and finally tended to be stable. The I_{corr} value increased rapidly for 1 h, then decreased rapidly for 2 h and then tended to be stable. The R_p value increased and then decreased for 10 h but increased rapidly after 10 h (Fig. 9c). The E_{corr} value of the sample #2 increased with the increase of
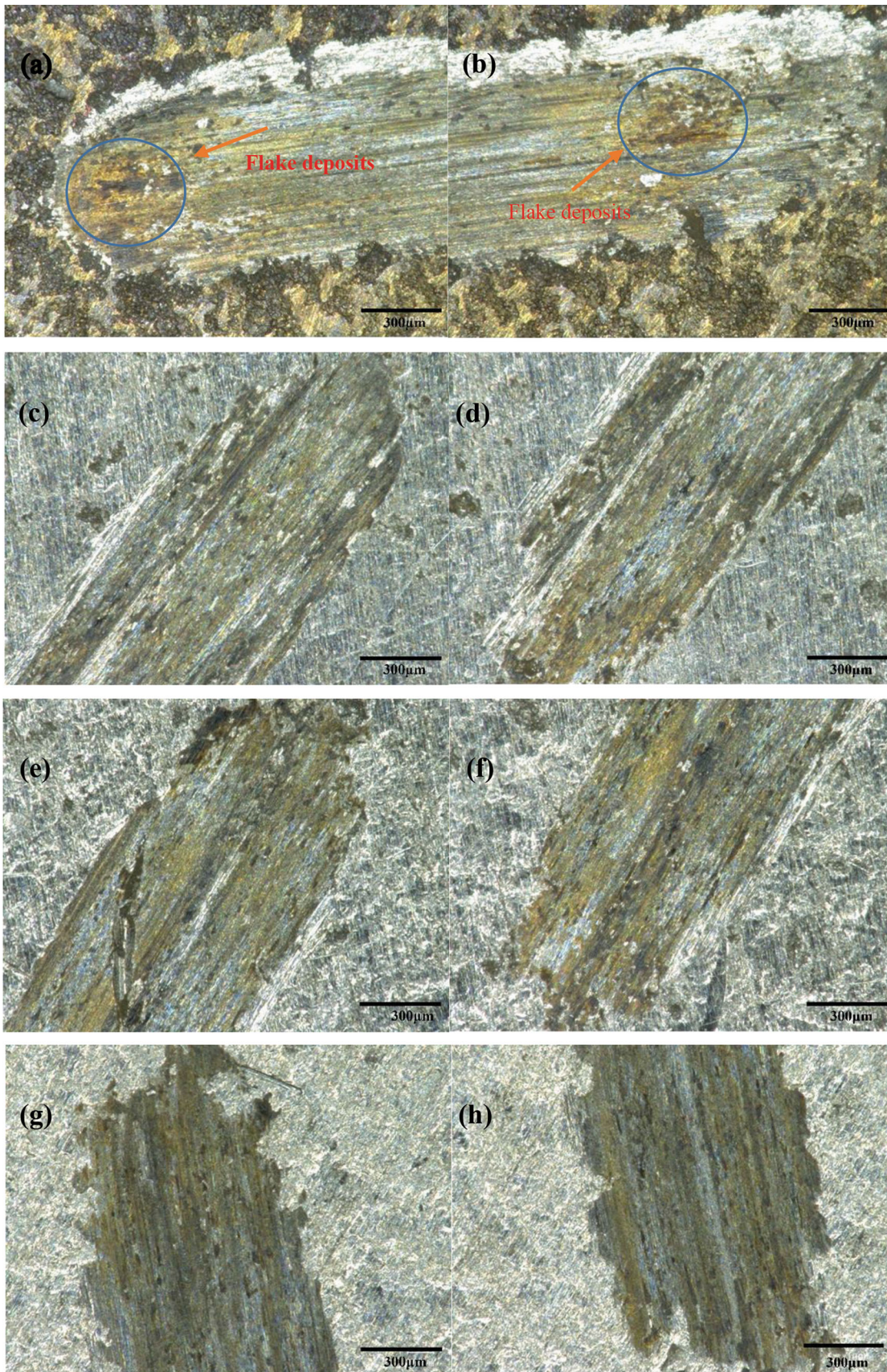
Fig. 6 Optical micrographs of scratches of samples with and without pre-strain deformation after wear test (a,b) 0%, (c,d) 5%, (e,f) 10%, and (g,h) 20%
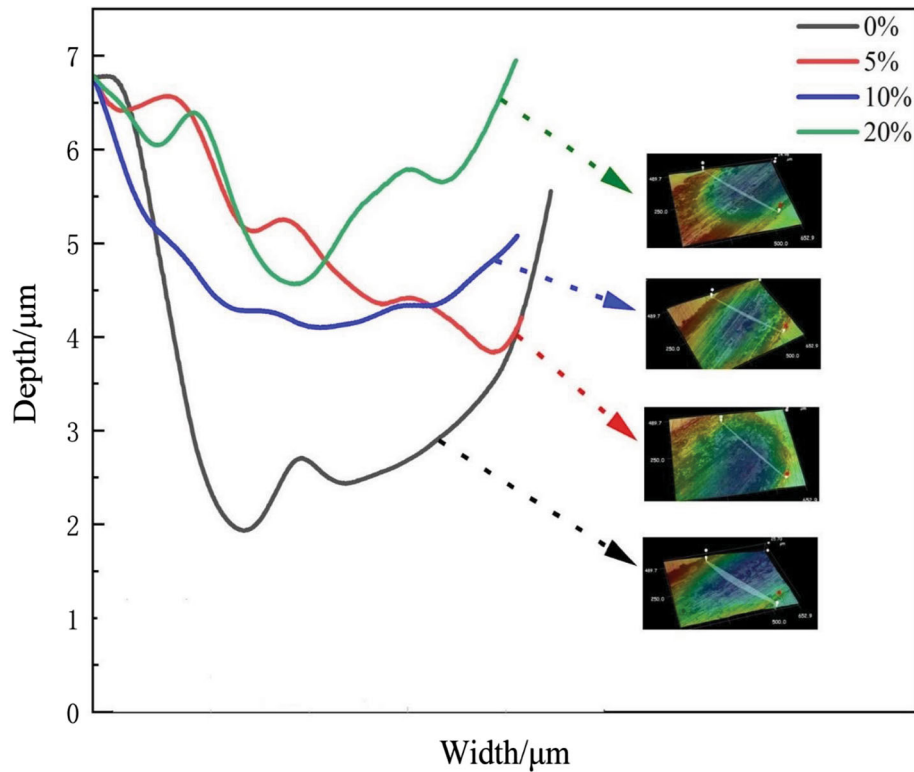
Fig. 7 The contour plots of samples with and without pre-strain deformation

Table 2 The depth and width of wear scratches on the surface of the sample after room temperature wear test

Samples	#0	#1	#2	#3
Condition	**Temperature: room temperature**			
	Friction type: reciprocating friction			
Depth/μm	5.164 ± 1.12	4.832 ± 0.8	4.163 ± 1.25	3.135 ± 0.91
Width/μm	204.6 ± 2.1	191.5 ± 3.56	190.4 ± 2.14	207.1 ± 1.12

soaking time, reached the highest value for 1 d, and then decreased after 3d. The I_{corr} and R_p values had almost no change. The E_{corr} value of sample #3 was the lowest for 1 h. The I_{corr} value had almost no change after immersion for $0 \sim 1$ h. The R_p value first increased and then decreased. The I_{corr} value of each sample shows almost no change and almost coincided in the corrosion solution after the immersion for 3 h due to the passivation effect from the formation of Cr oxides on the surface of the steel.

On the Nyquist diagram as shown in Figure 10, the larger the arc diameter is, the greater the hindrance is. In Fig. 10(a), the arc radius of sample #0 was the largest due to the lowest defects in the sample. The electrochemical impedance arc diameters of the other samples #1 to #3 after strain hardening were less than that of sample #0. Although the strain-hardened specimens showed high hardness and good wear resistance, the corrosion resistance of the specimens deteriorated due to the presence of some defects, such as an increase in dislocation density. From Fig. 10(b), it is found that the diameter of electrochemical impedance arc became smaller for sample #0

and larger for sample #3. In Fig. 10(c), the electrochemical impedance of sample #1 increased with the increase of soaking time of 3h, and then decreased and kept stable, which indicated that the passivation layer was relatively stable. In Fig. 10(d), the electrochemical impedance arc diameters of samples #1 #2 #3 did not differ significantly. From Fig. 10(e), the trend of sample #1 is found to be similar to that of sample #0, and the impedance arc diameters of #2 and #3 are slightly smaller than that of sample #0. As the immersion time increased, the electrochemical impedance arc diameter of sample #0 became smaller and then larger, which was attributed to the disruption of the passivation layer and then the re-formation of a new passivation layer, and the arc radius of sample #3 exceeded that of sample #0 after soaking for 3 days (See Fig. 10f). The electrochemical reactions are as follows:
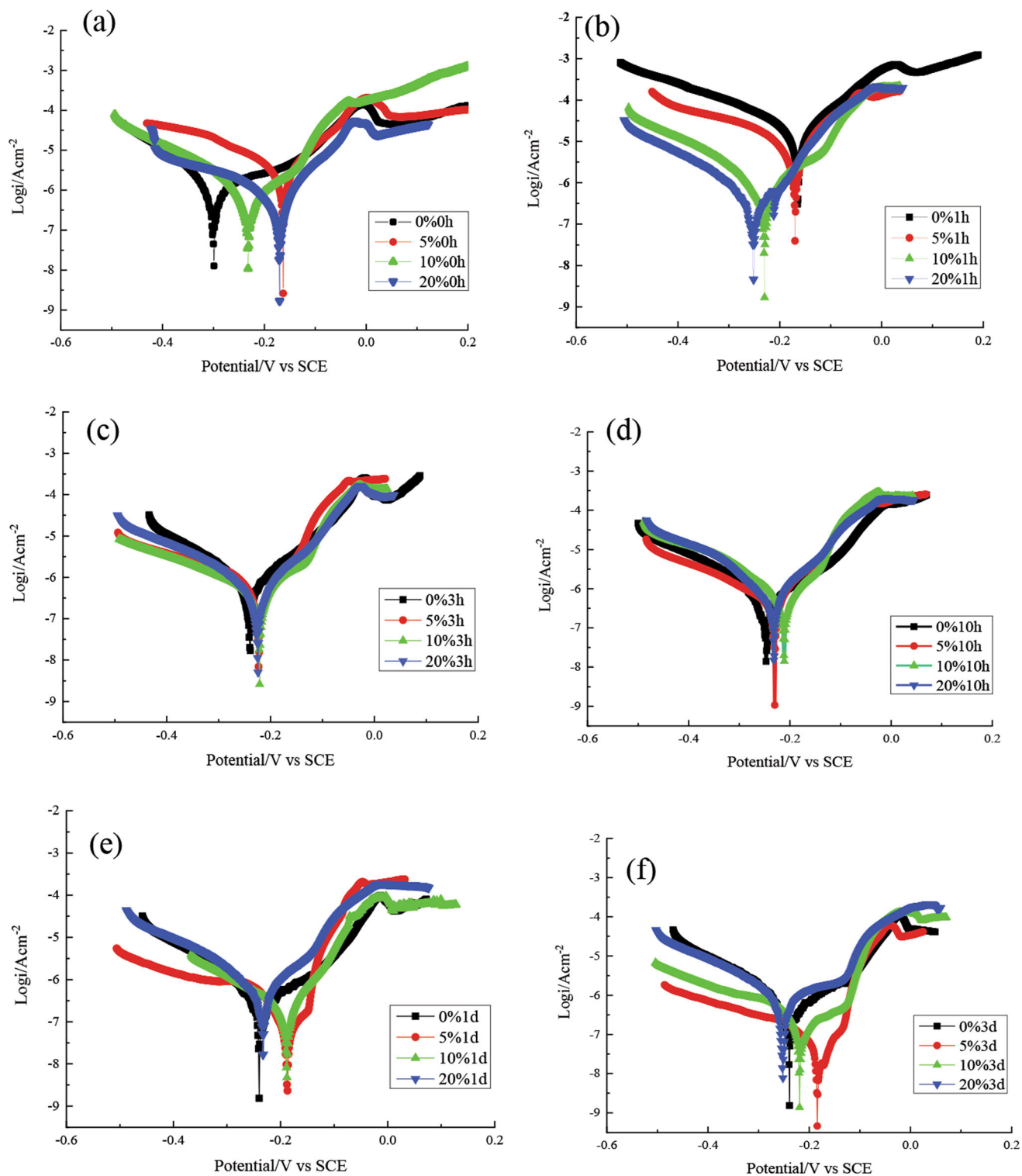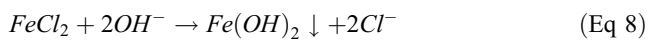
$$H_2O + \frac{1}{2}O_2 + 2e^- \rightarrow 2OH^- \qquad \text{(Eq 5)}$$

$$Fe^{2+} + 2OH^- \rightarrow Fe(OH)_2 \downarrow \qquad \text{(Eq 6)}$$

Fig. 8 Polarization curves of the samples in NaCl solution (a) 0 h, (b) 1 h, (c) 3 h, (d) 10 h, (e) 1d, (f) 3d

$$Fe^{2+} + 2Cl^- \rightarrow FeCl_2 \tag{Eq 7}$$

$$FeCl_2 + 2OH^- \rightarrow Fe(OH)_2 \downarrow + 2Cl^- \tag{Eq 8}$$

$$4Cr + 3O_2 \rightarrow 2Cr_2O_3 \tag{Eq 9}$$

After pre-strain deformation, the crystal structure in the sample is disordered at the grain boundary and the as-strained sample has high grain boundary energy (Ref 25). These sites are often the gathering places of impurities. Therefore, the grain boundary is often the origin point of electrochemical corrosion such as pitting. On the other hand, the local corrosion is the main failure site, and pitting corrosion is easy to occur in grain boundaries or heterogeneous structures (Ref 33, 34). From the

Table 3 Electrochemical corrosion parameters of 316L stainless steel (Self-corrosion voltage (E_{ccor}); Self-corrosion current (I_{ccor}); Polarization resistance (R_p))

Time	Sample	E_{ccor}/V	I_{ccor}/μA·cm^{-2}	R_p/Ω·cm^2
0 h	#0(0%)	−0.299	1.624	21362.17
	#1(5%)	−0.163	3.82	6956.9
	#2(10%)	−0.232	0.6955	33041.8
	#3(20%)	−0.161	2.366	11809.1
1 h	#0(0%)	−0.165	21.21	1406.3
	#1(5%)	−0.170	7.267	4108.6
	#2(10%)	−0.230	0.7935	35176.2
	#3(20%)	−0.251	0.3372	62746.3
3 h	#0(0%)	−0.239	0.8033	28364.2
	#1(5%)	−0.223	0.5681	43539.5
	#2(10%)	−0.221	0.4617	49132.3
	#3(20%)	−0.224	0.3909	53817.6
10 h	#0(0%)	−0.247	0.6314	39018.5
	#1(5%)	−0.230	0.6276	32166.5
	#2(10%)	−0.211	0.5693	29893.3
	#3(20%)	−0.232	0.5975	29587.0
1d	#0(0%)	−0.240	0.4018	56216.1
	#1(5%)	−0.187	0.1351	150258.5
	#2(10%)	−0.188	0.2274	77591.0
	#3(20%)	−0.233	0.5074	39891.5
3d	#0(0%)	−0.239	0.7706	38141.5
	#1(5%)	−0.184	0.06917	291418.2
	#2(10%)	−0.219	0.3152	90953.7
	#3(20%)	−0.252	1.320	34133.0

perspective of the improvement of breaking potential, twinning has good corrosion resistance compared with grain boundaries. This is because the formation of twinning after strain hardening reduces the grain boundary energy (Ref 35), reducing the adsorption capacity of chloride ions in twin crystals, which leads to a decrease in breaking potential (Ref 36). Therefore, the existence of twins can improve the corrosion resistance of the steel in a corrosive solution.

Table 4 displays the electrochemical impedance data of the simulated equivalent circuits. The equivalent circuit of sample #1 after soaking for 0 h and 3 days was R (Q(R(QR))) type (see Fig. 11a), where R_s was the solution resistance in 3.5% NaCl solution; and R_b and CPE_b were the charge transfer resistance and the capacitance between the solution and the passive layer and activated dissolution area at the bottom of etching hole, respectively and R_t and CPE_t were the resistance and capacitance of passive layer on the substrate surface, respectively. Therefore, it can be inferred that the surface of sample #1 after 5% pre-strain could be passivated again after soaking time for 3 days. However, the equivalent circuit of the other samples with different soaking times and pre-strain deformation values was R(QR) type (see Fig. 11b), where R_t and CPE_b represented the charge transfer resistance and the capacitance at the interface between the solution and the sample, respectively (Ref 37, 38). According to the above results from Tafel and Nyquist plots, sample #1 has significant benefits for anticorrosive properties due to high corrosion potential and high width of the capacitive loop (Ref 39). According to the above data and analysis, sample #1 had positive corrosion potential, the lowest corrosion current density, and a relatively large impedance, indicating the corrosion resistance of sample #1
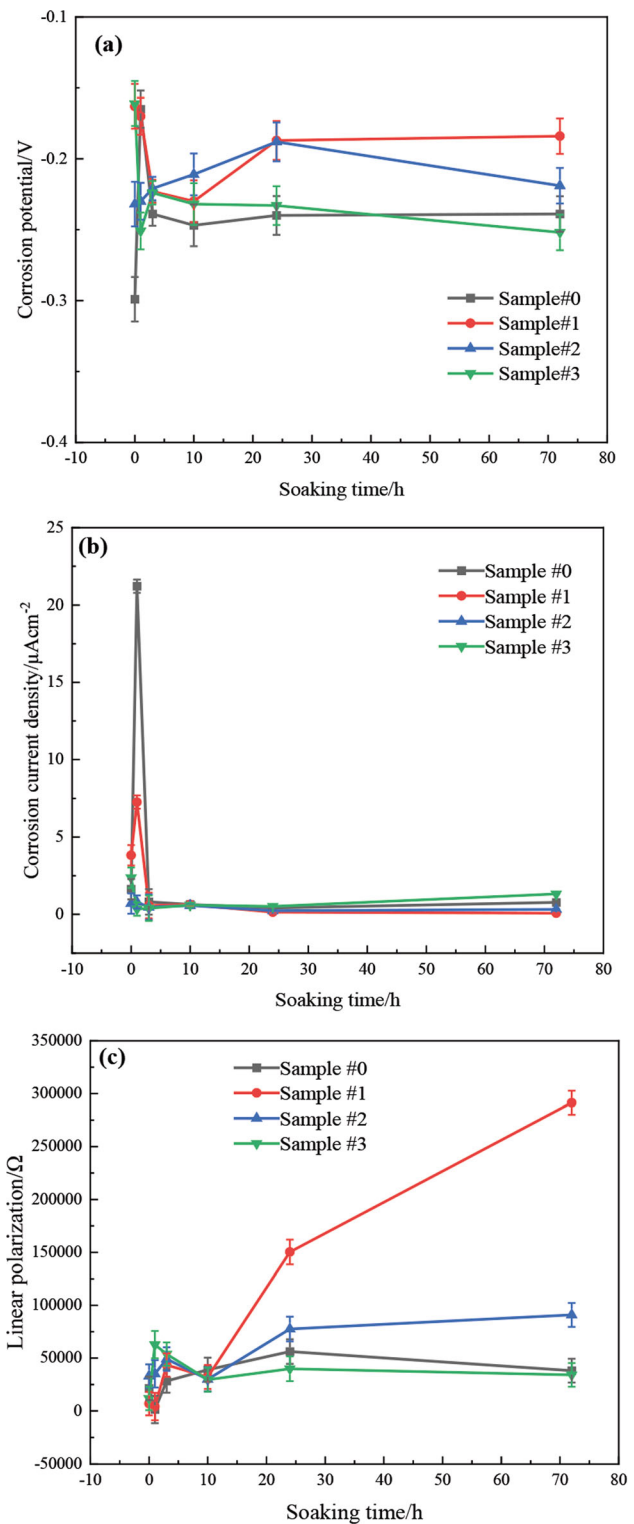

Fig. 9 Corrosion parameters of different pre-strained samples immersed in NaCl solution at room temperature for 0 h, 1 h, 3 h, 10 h, 1d, and 3d (a) Corrosion potential (b) Corrosion current density (c) Linear polarization

was the best in solution after soaking for 3 days, compared with other samples with strain hardening.
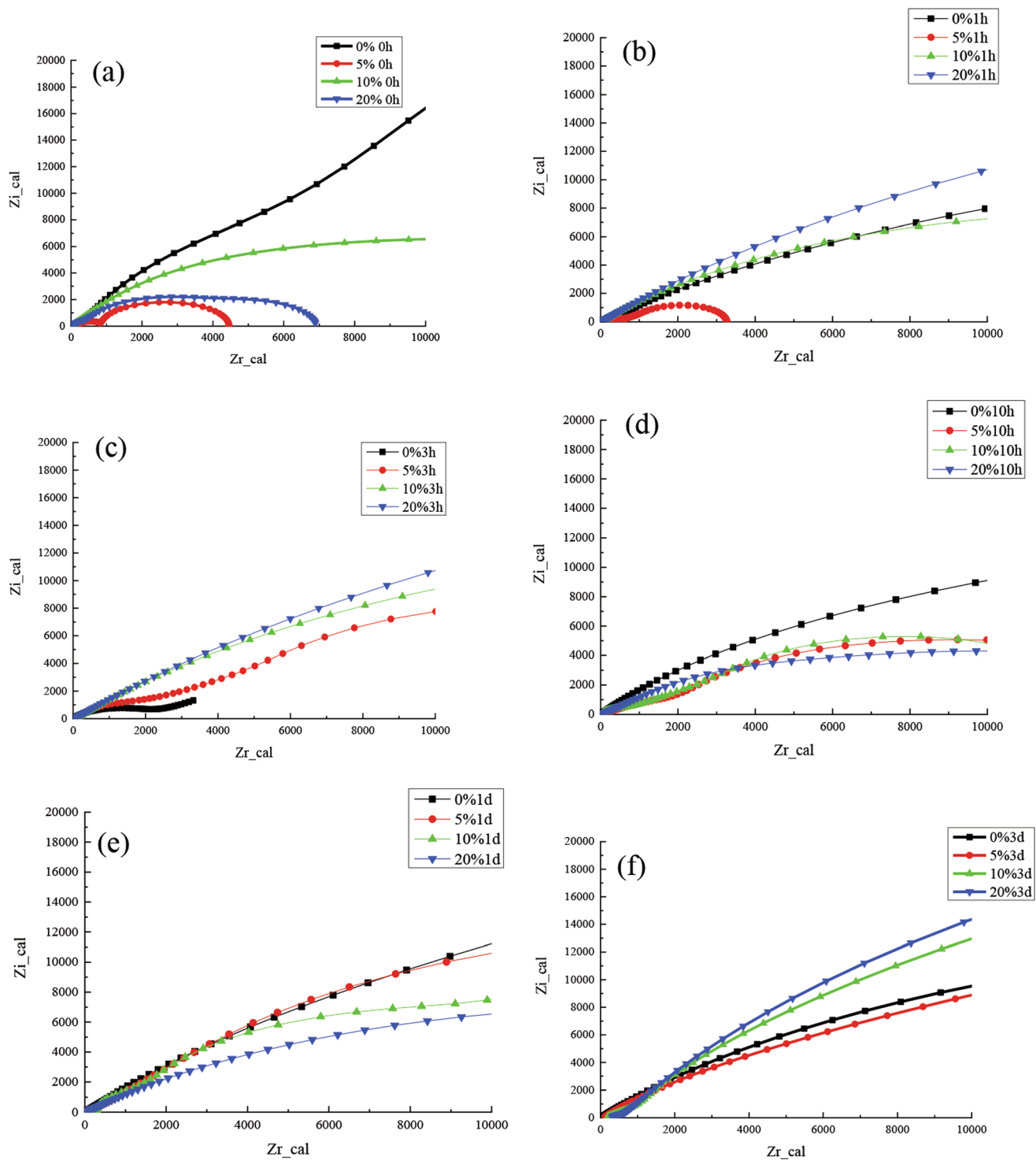
Fig. 10 EIS spectra of the samples with and without pre-strain deformation in NaCl solution (a) 0 h, (b) 1 h, (c) 3 h, (d) 10 h, (e) 1d, (f) 3d

4. Discussion

Figure 3 displays the microstructure of the pre-strained 316L steel at high magnification. It is noted that deformation twinning structures exist in pre-strained specimens. From optical micrographically observations, it is difficult to distinguish strain-induced martensite. Then, XRD or electron back-scattered diffraction (EBSD) technique could be conducted to find whether the martensite transformation existed in the pre-

strained samples. By equation calculation and XRD repeated analysis (see Fig. S1), the overall content of the phases did not change significantly by considering the range of the errors, indicating that the pre-strain at room temperature basically had no significant effect on the martensite transformation. Eskandari et al. (Ref 28) studied the influence of pre-strain at 250 °C on the strain-induced martensite transformation after cold rolling at 15 °C in 316L stainless steel and found that, with the pre-strain increasing to 30%, the volume fraction of martensite

Table 4 Impedance fitted circuit data of 316L stainless steel (the solution resistance in 3.5% NaCl solution (R_s); the charge transfer resistance and the capacitance between the solution (R_b); the resistance (R_t); the passive layer and activated dissolution area at the bottom of etching hole (CPE_b); the capacitance of passive layer on the substrate surface (CPE_t)

| Time	Sample	$R_s (\Omega cm^2)$	$R_b (\Omega cm^2)$	$R_t (\Omega cm^2)$	CPE_b	CPE_t
0 h	#0(0%)	8.48	3.017E16	…	8.73E−5	…
	#1(5%)	193.9	712.7	3549	5.39E−8	1.26E−6
	#2(10%)	7.083	2.348E4	…	1.13E−4	…
	#3(20%)	6.688	7570	…	6.21E−5	…
1 h	#0(0%)	1.244	6.815E4	…	1.01E−4	…
	#1(5%)	1.65	4080	…	5.74E−5	…
	#2(10%)	11.82	3.257E4	…	1.19E−4	…
	#3(20%)	7.288	7.499E4	…	7.64E−5	…
3 h	#0(0%)	20.7	1161	…	1.48E−5	…
	#1(5%)	13.01	2.505E4	…	1.52E−5	…
	#2(10%)	79.37	4.713E4	…	3.67E−6	…
	#3(20%)	5.584	9.618E4	…	6.24E−5	…
10 h	#0(0%)	10.75	4.471E4	…	1.28E−4	…
	#1(5%)	58.15	2.191E4	…	2.05E−5	…
	#2(10%)	0.0893	1.514E4	…	1.53E−5	…
	#3(20%)	6.463	2.014E4	…	8.76E−5	…
1d	#0(0%)	16.67	9.164E4	…	1.07E−4	…
	#1(5%)	31.18	8.576E4	…	5.05E−6	…
	#2(10%)	186.5	4.807E4	…	1.44E−6	…
	#3(20%)	5.923	3.188E4	…	8.14E−5	…
3d	#0(0%)	7.263	6.671E4	…	1.59E−4	…
	#1(5%)	80.15	1.461E4	3.957E5	1.24E−6	9.80E−6
	#2(10%)	190.6	1.038E5	…	4.15E−6	…
	#3(20%)	345.7	8.207E4	…	2.21E−6	…
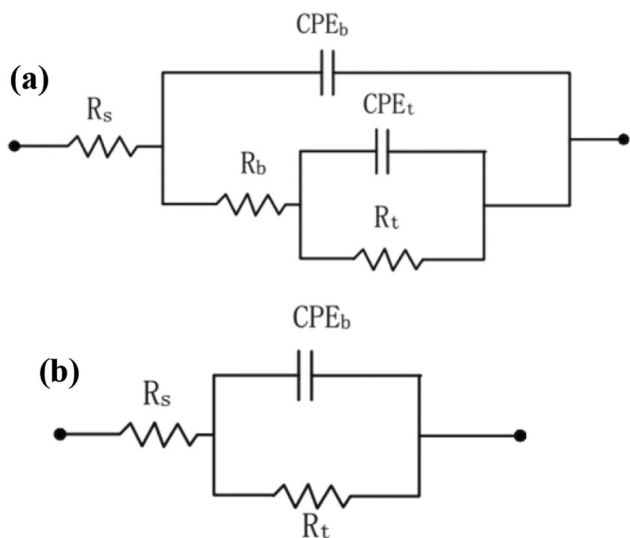
Fig. 11 Simulated equivalent circuits, (a) R (Q(R(QR))) type and (b) R(QR) type

increased from 55% to 70% with the hot rolling thickness reduction of 95%. However, the pre-strain deformation at room temperature did not significantly influence the content of martensite in 316L stainless steel (Ref 40), which has the same result in this study. Therefore, the main reason for the strengthening of 316L steel is ascribed to slip band and deformation twinning. Besides slip band and deformation twinning, dislocation density which would increase with pre-

strain deformation (Ref 41, 42), will also provide a strengthening effect, resulting in the increase in the hardness with pre-strain deformation. The higher dislocation density increases the microhardness of austenitic phase (Ref 43, 44). Secondly, due to the tensile pre-strain, the microstructure of 316L steel changes from equiaxed grains to slender grains with high aspect ratio (See Fig. 3e and f). It is known from the Hall-Petch relationship that the microhardness of the metal material can be enhanced by grain refinement (Ref 45, 46). The grain size of austenite is significantly refined during pre-strain, which increases the microhardness. Increased pre-strain implies a high dislocation density, which in turn, with the associated substructure, facilitates the nucleation of voids and microcracks that occurs under the influence of loading during wear testing (Ref 47). With increasing pre-strain, the random array of dislocations would tend to form stable dislocation cells (Ref 48). These would not tend to impede the nucleation of microvoids and microcracks during wear testing but would provide a higher resistance for their growth.

A certain degree of pre-strain can improve the corrosion resistance of 316L steel samples. After pre-deformation treatment, the strain concentration degree and dislocation density can become high, which has high internal energy and provides more stored energy for the growth of the passive films (Ref 49-51). The formation of corrosion channel in corrosion medium can be alleviated and the corrosion sensitivity can be reduced. The dynamic potential polarization curves of different pre-strained samples are shown in Fig. 8. The similar shape of the polarization curves under different pre-strain conditions shows that the pre-strain has no significant effect on the corrosion kinetics (Ref 52). In Fig. 9, the corrosion potentials and

corrosion current densities of samples with different pre-strain treatments are different. The maximum corrosion current density of the samples increases with the increase of strain hardening. For 0 h immersion time, the pre-strained sample #2 has better corrosion resistance because it has lower corrosion current density and higher polarization impedance values. The corrosion potential and corrosion current density of the samples changes with the increasing immersion time, which may be due to the process of destruction and regeneration of the passivation layer on the surface of the sample. After the pre-strain treatment, grain boundaries and dislocations of the samples affect their corrosion resistance. High dislocation density is detrimental for pitting resistance (Ref 53). In addition, grain boundaries are also prone to corrosion of the areas, as they are usually where impurities collect. The pitting corrosion of the pre-strained 316 L samples would be further studied in future. The equivalent circuit of sample #1 with pre-strain deformation of 5% after 3 days of immersion is a structure of type R (Q(R(QR))), where Rs represents the solution resistance in 3.5% NaCl solution, Rb and CPE_b represent the charge transfer resistance and capacitance between the solution and the area being etched and between the actively dissolved areas at the bottom of the etched holes, while Rt and CPE_t represent the passivation layer on the substrate surface of the resistance and capacitance. These characteristics and parameters illustrate the ability of sample #1 with pre-strain deformation of 5% to re-form the passivation layer after a certain immersion time. Also, the high corrosion potential, low corrosion current density and relatively large impedance are important factors for the good corrosion resistance of sample #1 with pre-strain deformation of 5%.

5. Conclusions

(1) As the pre-strain deformation increases, the surface and cross-sectional microhardness increases, with the sample with a pre-strain deformation of 20% having the greatest surface microhardness approximately 1.72 times higher than the unstrained microhardness, an increase of 0.72 times. When the pre-strain deformation is greater than 5%, the surface microhardness is greater than the cross-sectional microhardness.

(2) The wear resistance of 316L austenitic stainless steel was enhanced after pre-strain deformation. The friction coefficients of the samples gradually decreased with the increase of strain hardening values. Combining the friction coefficient and scratch depth, the smaller scratch depth and lower friction coefficient of the 20% pre-strained sample indicate that the 316L austenitic stainless steel with 20% pre-strain deformation has the best wear resistance.

(3) In 3.5 wt% NaCl solution, the corrosion resistance of the samples after strain hardening deteriorated for the immersion time of 0 days due to the existence of some defects. The corrosion resistance of 316L austenitic stainless steel with pre-strain deformation of 5% after soaking for 3 days was the best in as-strained samples.

References

1. K.H. Lo, C.H. Shek and J.K.L. Lai, Recent Developments in Stainless Steels, *Mater. Sci. Eng. R.*, 2009, **65**, p 39–104. https://doi.org/10.1016/j.mser.2009.03.001

2. J. Zheng, A. Guo, C. Miao et al., Cold Stretching of Cryogenic Pressure Vessels from Austenitic Stainless Steels, *Asme Pressure Vessels & Piping Conf.*, 2011, **1**, p 693–698. https://doi.org/10.1115/PVP2011-57331

3. H. Yu and X.D. Chen, Study and Application on Mechanical Behavior of Austenitic Stainless Steels Based on Cold Stretching Technology, *China Mech. Eng.*, 2011, **22**, p 2633–2637. https://doi.org/10.1016/S1872-5805(11)60064-4

4. W.S. Lee, C.F. Lin, T.H. Chen et al., High Temperature Microstructural Evolution of 304L Stainless Steel as Function of Pre-Strain and Strain Rate, *Mater. Sci. Eng. A.*, 2010, **527**, p 3127–3137. https://doi.org/10.1016/j.msea.2010.02.007

5. N.L. Parthasarathi and M. Duraiselvam, Improvement of High Temperature Wear Resistance of AISI 316 ASS Through NiCrBSiCFe Plasma Spray Coating, *J. Miner. Mater. Character. Eng.*, 2010, **9**, p 653–670. https://doi.org/10.4236/jmmce.2010.97047

6. M. Hua, X.C. Wei and J. Li, Friction and Wear Behavior of SUS 304 Austenitic Stainless Steel Against Al2O3 Ceramic Ball Under Relative High Load, *Wear*, 2008, **265**, p 799–810. https://doi.org/10.1016/j.wear.2008.01.017

7. Z.Y. Li, C. Qiu, C.B. Liu et al., The Mechanoelectrochemical Effect on the Electrochemical Corrosion of Austenitic Stainless Steel, *J. Mater. Res. Technol.*, 2023, **24**, p 1203–1215. https://doi.org/10.1016/j.jmrt.2023.03.030

8. S. Tokita, K. Kadoi, S. Aoki et al., Relationship Between the Microstructure and Local Corrosion Properties of Weld Metal in Austenitic Stainless Steels, *Corros. Sci.*, 2020, **175**, p 108867. https://doi.org/10.1016/j.corsci.2020.108867

9. S.M. Kumar, A.R. Kannan, R. Pramod et al., Microstructure and High Temperature Performance of 321 SS Wall Manufactured Through Wire-Arc Additive Manufacturing, *Mater. Lett.*, 2022, **314**, p 131913. https://doi.org/10.1016/j.matlet.2022.131913

10. D.X. Wen, P. Long, J.J. Li et al., Effects of Linear Heat Input on Microstructure and Corrosion Behavior of an Austenitic Stainless Steel Processed by Wire Arc Additive Manufacturing, *Vacuum*, 2020, **173**, p 109131. https://doi.org/10.1016/j.vacuum.2019.109131

11. Z.L. Zhang and T. Bell, Structure and Corrosion Resistance of Plasma Nitrided Stainless Steel, *Surf. Eng.*, 1985, **1**, p 131–136. https://doi.org/10.1179/sur.1985.1.2.131

12. S. Picard, J.B. Memet, R. Sabot et al., Corrosion Behaviour, Microhardness and Surface Characterisation of Low Energy, High Current ion Implanted Austenitic Stainless Steel, *Mater. Sci. Eng. A.*, 2001, **303**, p 163–172. https://doi.org/10.1016/S0921-5093(00)01841-4

13. M. Lindroos, M. Apostol, V. Heinoet et al., The Deformation, Strain Hardening, and Wear Behavior of Chromium-Alloyed Hadfield Steel in Abrasive and Impact Conditions, *Toxicol. Lett.*, 2015, **57**, p 24. https://doi.org/10.1007/s11249-015-0477-6

14. P.L. Ko, G. Knowles and M.C. Taponat, Friction Characteristics and the Wear Process of Metal Pairs in Sliding Contacts—with Applications to Modelling Wear of Power Plant Components, *Wear*, 1997, **213**, p 148–158. https://doi.org/10.1016/S0043-1648(97)00169-5

15. X.B. Xu, Z. Ling, X. Wu et al., Martensitic Transformation and Work Hardening of Metastable Austenite Induced by Abrasion in Austenitic Fe-C-Cr-Mn-B Alloy - a TEM Study, *Mater. Sci. Technol.*, 2002, **18**, p 1561–1564. https://doi.org/10.1179/026708302225007466

16. S. Ningshen and U. Kamachi Mudali, Pitting and Intergranular Corrosion Resistance of AISI Type 301LN Stainless Steels, *J. Mater. Eng. Perform.*, 2010, **19**, p 274–281. https://doi.org/10.1007/s11665-009-9441-7

17. G. Suresh, P.K. Parida, S. Bandiet et al., Effect of Carbon Content on the Low Temperature Sensitization of 304L SS and its Corrosion Resistance in Simulated Ground Water, *Mater. Chem. Phys.*, 2019, **226**, p 184–194. https://doi.org/10.1016/j.matchemphys.2019.01.019

18. V. Kain, S.S. Shinde and H.S. Gadiyar, Mechanism of Improved Corrosion Resistance of Type 304L Stainless Steel, Nitric Acid Grade, in Nitric Acid Environments, *J. Mater. Eng. Perform.*, 1994, **3**, p 699–705. https://doi.org/10.1007/BF02818368

19. G. Shit, M.V. Kuppusamy and S. Ningshen, Corrosion Resistance Behavior of GTAW Welded AISI Type 304L Stainless Steel, *Trans. Indian Inst. Met.*, 2019, **72**, p 2981–2995. https://doi.org/10.1007/s12666-019-01779-w

20. A. Ravi Shankar, S.S. Babu, M. Ashfaq et al., Dissimilar Joining of Zircaloy-4 to Type 304L Stainless Steel by Friction Welding Process, *J. Mater. Eng. Perform.*, 2009, **18**, p 1272–1279. https://doi.org/10.1007/s11665-009-9376-z

21. R. Sundar, P. Ganesh, B.S. Kumar et al., Mitigation of Stress Corrosion Cracking Susceptibility of Machined 304L Stainless Steel Through Laser Peening, *J. Mater. Eng. Perform.*, 2016, **25**, p 3710–3724. https://doi.org/10.1007/s11665-016-2220-3

22. G. Shit, P. Bhaskar, S. Ningshen et al., Phase Transition of AISI Type 304L Stainless Steel Induced by Severe plastic Deformation Via Cryo-Rolling, *AIP Conf. Proceed.*, 2017, **1832**, p 030020. https://doi.org/10.1063/1.4980199

23. C.H. Hsu, T.C. Chen, R.T. Huang et al., Stress Corrosion Cracking Susceptibility of 304L Substrate and 308L Weld Metal Exposed to a Salt Spray, *Mater*, 2017, **10**, p 187. https://doi.org/10.3390/ma10020187

24. J. Peng, K. Li, J. Peng et al., The Effect of Pre-Strain on Tensile Behaviour of 316L Austenitic Stainless Steel, *Mater. Sci. Technol.*, 2018, **34**, p 547–560. https://doi.org/10.1080/02670836.2017.1421735

25. J. Peng, K. Li, Q. Gao et al., Estimation of Mechanical Strength for Pre-Strained 316L Austenitic Stainless Steel by Small Punch Test, *Vacuum*, 2019, **160**, p 37–53. https://doi.org/10.1016/j.vacuum.2018.11.015

26. J. Peng, Y. Wang, Q. Dai et al., Effect of Stress Triaxiality on Plastic Damage Evolution and Failure Mode for 316L Notched Specimen, *Vacuum*, 2019, **9**, p 1067. https://doi.org/10.1016/j.vacuum.2018.11.015

27. K.S. Li and J. Peng, Effect of Pre-Strain on Small Punch Creep Test of 316L Stainless Steel at 373K, *Key Eng. Mater.*, 2019, **795**, p 152–158

28. M. Eskandari, A. Najafizadeh and A. Kermanpur, Effect of Strain-Induced Martensite on the Formation of Nanocrystalline 316L Stainless Steel after cold Rolling and Annealing, *Mater. Sci. Eng. A*, 2009, **519**, p 46–50. https://doi.org/10.1016/j.msea.2009.04.038

29. G. Sha, Y.B. Wang, X.Z. Liao et al., Influence of Equal-Channel Angular Pressing on Precipitation in an Al-Zn-Mg-Cu Alloy, *Acta Mater.*, 2009, **57**, p 3123–3132. https://doi.org/10.1016/j.actamat.2009.03.017

30. M. Federici, G. Perricone, S. Gialanella et al., Sliding Behaviour of Friction Material Against Cermet Coatings: Pin-On-Disc Study of the Running-in Stage, *Tribol. Lett.*, 2018, **66**, p 1–11. https://doi.org/10.1007/s11249-018-1004-3

31. Y. Sun, R. Bailey and A. Moroz, Surface Finish and Properties Enhancement of Selective Laser Melted 316L Stainless Steel by Surface Mechanical Attrition Treatment, *Surf. Coat. Technol.*, 2019, **378**, p 124993. https://doi.org/10.1016/j.surfcoat.2019.124993

32. J.P. Riviére, C. Brin and J.P. Villain, Structure and Topography Modifications of Austenitic Steel Surfaces After Friction in Sliding Contact, *Appl. Phys. A*, 2003, **76**, p 277–283. https://doi.org/10.1007/s00339-002-1481-x

33. M.A. Baker and J.E. Castle, The Initiation of Pitting Corrosion at MnS Inclusions, *Corros. Sci.*, 1993, **34**, p 667–682. https://doi.org/10.1016/0010-938X(93)90279-P

34. M.A. Baker and J.E. Castle, The Initiation of Pitting Corrosion of Stainless Steels at Oxide Inclusions, *Corros. Sci.*, 1992, **33**, p 1295–1312. https://doi.org/10.1016/0010-938X(92)90137-R

35. R.L. Fullman, Formation of Annealing Twins During Grain Growth, *J. Appl. Phys.*, 1951, **22**, p 1350–1355. https://doi.org/10.1063/1.1699865

36. G. Meng, F. Sun, Y. Shao et al., Influence of Nano-Scale Twins (NT) Structure on Passive Film Formed on Nickel, *Electrochim. Acta.*, 2010, **55**, p 2575–2581. https://doi.org/10.1016/j.electacta.2009.12.027

37. W.P. Wu, G.Q. Sun, Q.Q. Wang et al., Preparation, Wear Resistance, and Corrosion Performance of arc-Sprayed Zn, Al, and Zn-Al Coatings on Carbon Steel Substrates, *J. Mater. Eng. Perform.*, 2023 https://doi.org/10.1007/s11665-023-07889-3

38. Z. Jia, C. Du, C. Li et al., Study on Pitting Process of 316L Stainless Steel by Means of Staircase Potential Electrochemical Impedance Spectroscopy, *Int. J. Min. Met. Mater.*, 2011, **18**, p 48–52. https://doi.org/10.1007/s12613-011-0398-9

39. W.P. Wu, J.W. Liu, Y. Zhang et al., Electrochemical Characteristics of Iridium Coating by Double Glow Plasma Discharge Process on Titanium Alloy Substrates, *Surf. Eng.*, 2019, **35**, p 954–961. https://doi.org/10.1080/02670844.2019.1579400

40. Zhang ZJ (2014) Experimental research on the effect of strain hardening on stress corrosion of 304 and 316L austenitic stainless steel, PhD dissertation, Zhejiang University of Technology, 2014 (In Chinese)

41. O. Bouaziz and N. Guelton, Modelling of TWIP Effect on Work-Hardening, *Mater. Sci. Eng. A.*, 2001, **319–321**, p 246–249. https://doi.org/10.1016/S0921-5093(00)02019-0

42. K.P. Staudhammer and L.E. Murr, The Effect of Prior Deformation on the Residual Microstructure of Explosively Deformed Stainless Steels, *Mater. Sci. Eng.*, 1980, **44**, p 97–113. https://doi.org/10.1016/0025-5416(80)90235-9

43. Z.Q. Zhang, H.Y. Jing, L.Y. Xu et al., Microstructural Characterization and Electron Backscatter Diffraction Analysis Across the Welded Interface of Duplex Stainless Steel, *Appl. Surf. Sci.*, 2017, **413**, p 327–343. https://doi.org/10.1016/j.apsusc.2017.03.301

44. L.H. Han, T. Han, G.X. Chen et al., Influence of Heat Input on Microstructure, Hardness and Pitting Corrosion of Weld Metal in Duplex Stainless Steel Welded by Keyhole-TIG, *Mater. Charact.*, 2021, **175**, p 111052. https://doi.org/10.1016/j.matchar.2021.111052

45. M. Hajian, A. Abdollah-zadeh, S.S. Rezaei-Nejad et al., Microstructure and Mechanical Properties of Friction Stir Processed AISI 316L Stainless Steel, *Mater. Des.*, 2015, **67**, p 82–94. https://doi.org/10.1016/j.matdes.2014.10.082

46. F.J. Cao, G.Q. Huang, W.T. Hou et al., Simultaneously Enhanced Strength-Ductility Synergy and Corrosion Resistance in Submerged Friction Stir Welded Super Duplex Stainless Steel Joint Via Creating Ultrafine Microstructure, *J. Mater. Process. Technol.*, 2022, **307**, p 117660. https://doi.org/10.1016/j.jmatprotec.2022.117660

47. K.K. Ray, V. Toppo and S.B. Singh, Influence of Pre-Strain on the Wear Resistance of a Plain Carbon Steel, *Mater. Sci. Eng. A.*, 2006, **420**, p 333–341. https://doi.org/10.1016/j.msea.2006.01.093

48. M. Nabil Bassim and M.R. Bayoumi, The Observation of Dislocation Structures during the Fracture of Prestrained AISI 4340 Steel, *Mater. Sci. Eng.*, 1986, **81**, p 317–324. https://doi.org/10.1016/0025-5416(86)90271-5

49. W.Y. Wang, Q.L. Pan, X.D. Wang et al., Effect of Laser Shock Peening on Corrosion Behaviors of Ultra-High Strength Al-Zn-Mg-Cu Alloys Prepared by Spray Forming and Ingot Metallurgy, *Corros. Sci.*, 2022, **205**, p 110458. https://doi.org/10.1016/j.corsci.2022.110458

50. S.A. Zakaria, A.S. Anayida, H. Zuhailawati et al., Characterization of Mechanical and Corrosion Properties of Cryorolled Al 1100 Alloy: Effect of Annealing and Solution Treatment, *T. Nonferr. Metal Soc.*, 2021, **31**, p 2949–2961. https://doi.org/10.1016/S1003-6326(21)65705-9

51. A. Balyanov, J. Kutnyakova, N.A. Amirkhanova et al., Corrosion Resistance of Ultra Fine-Grained Ti, *Scr. Mater.*, 2004, **51**, p 225–229. https://doi.org/10.1016/j.scriptamat.2004.04.011

52. H. Luo, C.F. Dong, X.G. Li et al., The electrochemical Behaviour of 2205 Duplex Stainless Steel in Alkaline Solutions with Different pH in the Presence of Chloride, *Electrochimi. Acta.*, 2012, **64**, p 211–220. https://doi.org/10.1016/j.electacta.2012.01.025

53. K. Kishore, A.K. Chandan, B.K. Sahoo et al., Novel observation of dominant role of strain rate over strain during pre-straining on corrosion behaviour of 304L austenitic stainless steel, *Mater. Chem. Phys.*, 2022, **277**, p 125522. https://doi.org/10.1016/j.matchemphys.2021.125522